How to cite:
doi.org/10.1002/anie.202303527

Gas Separation Hot Paper

Linker Vacancy Engineering of a Robust ftw-type Zr-MOF for Hexane Isomers Separation

Fu-An Guo[+], Jing Wang[+], Cailing Chen[+], Xinglong Dong, Xingyu Li, Hao Wang, Peng Guo,* Yu Han, and Jing Li**

Abstract: Discrimination of physically similar molecules by porous solids represents an important yet challenging task in industrially relevant chemical separations. Precisely controlled pore dimension and/or tailored pore surface functionality are crucial to achieve high-efficiency separation. Metal-organic frameworks (MOFs) are promising candidates for these challenging separations in light of their structural diversity as well as highly adjustable pore dimension/functionality. We report here a microporous, **ftw**-type Zr-based MOF structure, HIAM-410 (HIAM = Hoffmann Institute of Advanced Materials), built on hexanuclear Zr_6 cluster and pyrene-1,3,6,8-tetracarboxylate (ptc^{4-}). Its crystallographic structure has been determined using continuous rotation electron diffraction (cRED) technique combined with Rietveld refinement against powder X-ray diffraction data, aided by low-dose high-resolution transmission electron microscopy (HRTEM) imaging. The compound features exceptional framework stability that is comparable to the prototype MOF UiO-66. Interestingly, the linker vacancies in the pristine MOF structure could be partially restored by post-synthetic linker insertion. Its separation capability of hexane isomers is enhanced substantially upon the linker vacancy engineering. The restored structure exhibits efficient splitting of monobranched and dibranched hexane isomers at both room temperature and industrially relevant temperature.

Introduction

Industrially relevant hydrocarbon separations are critical for the production of a variety of extensively-used commodities, such as plastics, gasoline, and drugs.[1] These separation processes, currently dominated by heat-driven distillations, require tremendous energy input. Separation accomplished through selective physisorption by porous materials under mild conditions holds strong potential to reduce the associated energy consumption and suppress carbon dioxide emission. Traditional adsorbents have found uses in the industrial separation of hydrocarbons. For example, zeolite 5A is currently used for extracting linear alkanes from light naphtha, and Y zeolite is widely applied for the separation of xylenes.[2,3] However, certain challenging separations involving full discrimination of physically similar molecules such as olefin/paraffin or monobranched/dibranched alkanes remain to be daunting.[4] Adsorptive separation of these hydrocarbons of high similarity has stringent requirements on the structure, pore dimension, and functionality of the adsorbent, which have not been fully fulfilled by traditional materials. In this context, MOFs assembled through coordination of inorganic clusters and organic linkers are particularly promising for discriminating similar molecules, because of their structural diversity, high porosity, exceptional tunability with respect to their pore dimensions, and functionality.[5–7]

MOFs have demonstrated great promise in efficient separation of industrially relevant hydrocarbon mixtures such as propane/propylene,[8–11] ethane/ethylene,[12,13] xylene isomers,[14] etc., thanks to the successful practice of reticular chemistry which allows one to precisely tailor their pore structure and functionality. Fine-tuning of MOF structures is typically accomplished by making use of three strategies: linker engineering, metal/SBU engineering, and linker conformation engineering.[15] Linker engineering has been

[*] F.-A. Guo,[+] X. Li, Prof. H. Wang, Prof. J. Li
Hoffmann Institute of Advanced Materials, Shenzhen Polytechnic
7098 Liuxian Boulevard, Shenzhen, Guangdong 518055 (P. R. China)
E-mail: wanghao@szpt.edu.cn
Dr. J. Wang,[+] Prof. P. Guo
National Engineering Research Center of Lower-Carbon Catalysis Technology, Dalian Institute of Chemical Physics, Chinese Academy of Sciences
Dalian 116023 (China)
E-mail: pguo@dicp.ac.cn
Dr. C. Chen,[+] Dr. X. Dong, Prof. Y. Han
Advanced Membranes and Porous Materials Center, Physical Sciences and Engineering Division, King Abdullah University of Science and Technology
Thuwal, 23955-6900 (Saudi Arabia)
Prof. P. Guo
University of Chinese Academy of Sciences
Beijing 100049 (China)
Prof. J. Li
Department of Chemistry and Chemical Biology, Rutgers University
123 Bevier Road, Piscataway, NJ-08854 (USA)
E-mail: jingli@rutgers.edu
[+] These authors contributed equally to this work.

extensively practiced to achieve MOFs with tailored structure, porosity, pore size and functionality, as exemplified by IRMOFs,[16] MOF-74 analogues,[17] and UiO series,[18] to name a few. By using organic linkers with different dimensions and/or functionality, pore size, and surface chemistry of MOFs can be systematically adjusted with the overall connectivity remaining unaltered. Metal/SBU engineering has been applied where metal ions with similar coordination habit can be replaced by each other, as demonstrated in M_2(dobdc) (M = Mg, Mn, Fe, Co, Ni, Zn)[19] and M_6-**fcu**/**ftw**-MOF (M = Zr, Y, etc.).[20] Judicious selection of metal/SBU may render optimal pore size or framework charge for target applications. Achieving tailored structural features of MOFs by linker conformation engineering has not been documented until recently. Zhou, Farha, Liu, Wang, and co-workers have demonstrated the formation of different structures by controlling linker confirmation through optimization of synthetic conditions, which has largely enriched MOF structural diversity.[15,21–23] Besides the aforementioned three strategies involving pre-synthetic design and synthetic optimization, the pore structure and functionality of MOFs could also be tailored through post-synthetic modifications (PSM), including pore space partition,[24,25] ligand insertion,[26,27] and others. In particular, Zr-based MOFs (Zr-MOFs) built on hexanuclear Zr_6 clusters with a connectivity less than 12 (full connectivity) are prominent platforms for linker installation and post-synthetic fine-tuning of pore functionality. These ordered pockets in the crystal lattice with coordinately unsaturated metal centers can be filled with judiciously selected secondary linkers.[27] Additionally, Zr-MOFs built on 12-connected Zr_6 clusters are also commonly linker-deficient, with linker vacancy sites which are disordered in long range. These linker vacancies may notably influence the porosity, pore size, and surface functionality of the structure and can be potentially engineered for target applications.[28] Previous studies focused mainly on linker vacancy engineering of the prototype UiO-type MOFs while exploration for Zr-MOFs built on 12-c Zr_6 cluster and tetratopic linkers is more challenging and has not been well documented.[29–31]

In this work, we report the synthesis and structure of a **ftw**-type Zr-MOF, HIAM-410 built on 12-connected $Zr_6O_4(OH)_4(COOH)_{12}$ SBU and ptc^{4-}. The crystallographic structure of nanosized HIAM-410 was determined by combining cRED and Rietveld refinement against the powder X-ray diffraction (PXRD) data. HIAM-410 features exceptional stability under harsh conditions which is comparable to that of UiO-66. Interestingly, the as-synthesized HIAM-410 possesses notable linker vacancy sites, making its effective pore aperture noticeably larger than the predicted value from its vacancy-free idealized crystal structure (designated as HIAM-410VF, Figure 1). However, the vacancies can be partially restored by post-synthetic ptc^{4-} installation so as to adjust the pore dimensions of the MOF, as evidenced by Rietveld structure refinement before and after linker vacancy engineering. The post-synthetically linker-inserted HIAM-410 (denoted as HIAM-410LI) exhibits full discrimination of linear, monobranched, and dibranched hexane isomers through a synergistic effect of thermodynamically and kinetically driven mechanism.

Results and Discussion

Zr-MOFs, in particular those built on 12-connected Zr_6 clusters and small-sized organic linkers, feature highly

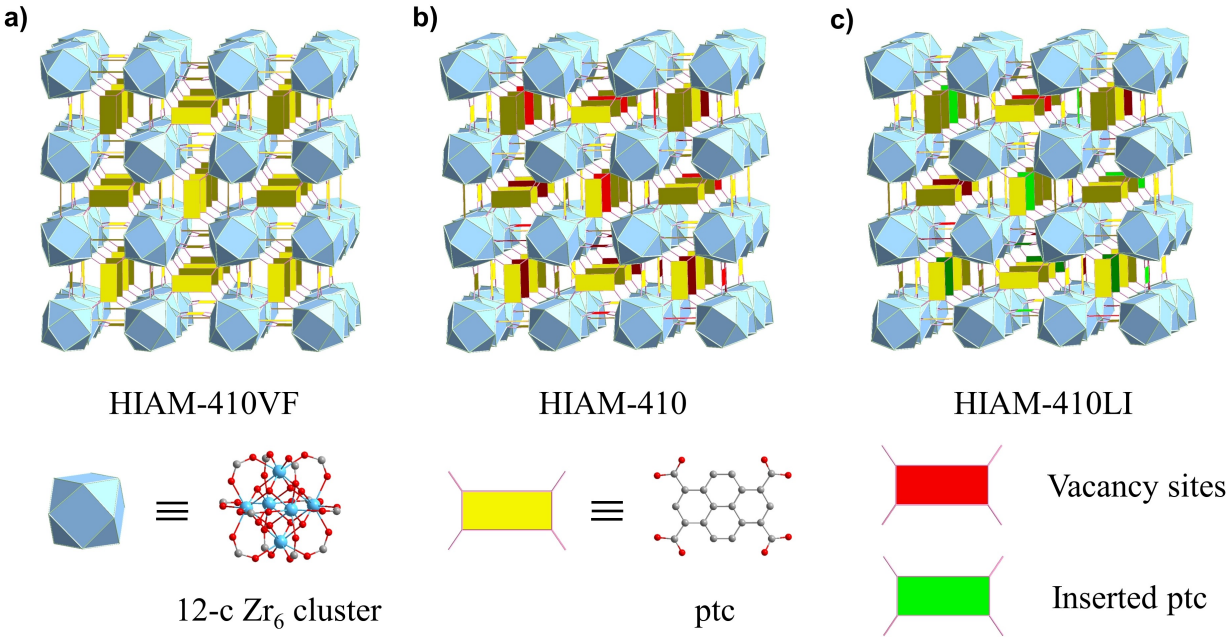

Figure 1. Schematic representation of linker vacancy engineering. a) Linker vacancy free structure of HIAM-410 (HIAM-410VF), b) Structure of as-synthesized HIAM-410, and c) Structure of HIAM-410 upon linker insertion (HIAM-410LI).

robust structures rendering them broad applicability for industrial utilizations.[32] A prominent example is UiO-66 constructed from $Zr_6O_4(OH)_4(COO)_{12}$ and terephthalate, with a **fcu** topology.[18] A number of studies have demonstrated that it possesses exceptional thermal, moisture, water, and hydrothermal stability, with its crystallinity and porosity well preserved upon treatment under harsh conditions. We also reported a 12-connected **ftw**-type Zr-MOF made of $Zr_6O_4(OH)_4(COO)_{12}$ and 3,3′,5,5′-biphenyltetracarboxylate ($bptc^{4-}$) that exhibits extraordinarily high stability.[33] Studies have revealed that topology and stability of MOFs are closely related to the connectivity of the Zr_6 SBU, which is determined by the geometry of the organic linkers. Tetracarboxylate linkers with a geometry close to a square are prone to forming **ftw** topology with 12-connected SBU, which features robust framework, large cavity and small pore aperture that are particularly promising for molecular separation. With this in mind, we selected a small-sized tetratopic linker, ptc^{4-} to target a stable **ftw**-type Zr-MOF. It appears a general fact that highly robust structures are always challenging to form large crystals, as seen in the case of UiO-66 and MIL-101(Cr). Similarly, in this case, despite tremendous efforts, growing crystals that are large enough for conventional single-crystal X-ray diffraction analysis was not successful. However, highly crystalline products with particle size of 50–100 nm could be easily obtained by solvothermal reactions of $ZrCl_4$ and H_4ptc in DMF/formic acid (Figure S1). Therefore, we applied the advanced cRED for the initial structure solution.[34] This technique enables us to collect 3D electron diffraction from one nanocrystal of interest, in this case, the unit cell parameters, space group, and even the atomic coordinates could be deduced from cRED data (Figure 2a–c). Its crystallographic structure is solved by cRED based on the space group *Im*-3 and also confirmed by Rietveld refinement against PXRD data (Figure S2). As expected, the obtained MOF, HIAM-410, is built on 12-connected $Zr_6O_4(OH)_4(COO)_{12}$ clusters, featuring 4,12-c **ftw** topology (Figure S3 and S4). The structure contains cubic cage-like pores where the vertexes of the cubes are occupied by the Zr_6 clusters and ptc^{4-} linkers take up the faces. The large-sized cages are interconnected by narrow windows with a diameter of $\approx$4 Å. It should be noted that, from the Rietveld refinement results, the occupancy of the organic linker ptc^{4-} (C1, C2, C3, C8, and C10) in the as-synthesized structure is 81.5 %, meaning that 18.5 % of the linker sites in the crystal lattice are vacant.

The structure of HIAM-410 was further analyzed by low-dose HRTEM imaging. HRTEM was performed under ultra-low electron dose conditions to prevent structural damage of the MOF by electron irradiation. The obtained HRTEM image revealed the high crystallinity of HIAM-410 (Figure 2d–h). The corresponding Fourier transform confirmed that it is of the HIAM-410 structure oriented along the ⟨001⟩ direction (Figure 2d). The HRTEM image was processed by correcting the effect of the contrast transfer function (CTF) of the objective lens to make the image contrast more interpretable. The CTF-corrected image displayed in Figure 2e matches perfectly with the simulated ⟨001⟩—projected electrostatic potential map of HIAM-410VF (Figure 2f) and the structure model obtained from cRED (Figure 2h). Our initial attempt of direct imaging of the linker vacancies failed, probably because they are randomly distributed in the crystal lattice without long-range order. Nevertheless, the HRTEM image further confirmed its crystallographic structure solved by cRED technique.

The phase purity of the as-synthesized HIAM-410 was confirmed by PXRD where the pattern agreed well with the simulated one (Figure 3b). Thermogravimetric analysis (TGA) displayed an initial weight loss of 18 % before 100 °C corresponding to the free solvents inside the pore, which is followed by a plateau up to 400 °C, indicating high thermal stability of the compound (Figure S5).

The porosity of HIAM-410 was evaluated by N_2 adsorption at 77 K. The adsorption-desorption isotherm displayed a typical Type I profile, indicating its microporous nature (Figure 3a). The calculated BET surface area and pore volume of HIAM-410 are 832 $m^2 g^{-1}$ and 0.42 $cm^3 g^{-1}$, respectively. We anticipated HIAM-410 constructed on 12-connected hexanuclear Zr_6 SBU and small-sized rigid tetratopic linker tpc^{4-} would possess high framework stability, similar to UiO-66 and Zr-bptc. This was experimentally confirmed by stability tests under various conditions. Temperature-variable in situ PXRD analysis indicated the crystallinity of the compound can be fully reserved up to 400–450 °C (Figure S6). Upon heating at 150 °C in open air, the crystal structure of HIAM-410 was also well-retained, indicating high thermal stability of the material (Figure 3b). Its chemical stability was systematically evaluated as well. It is stable in common organic solvents including methanol, ethanol, acetone, DCM, and hexane (Figure S7). It can also survive in highly acidic condition such as pH 0 aqueous solution (Figure 3b). Hydrothermal stability of HIAM-410 was further investigated and compared with that of the other benchmark MOFs including UiO-66, UiO-67, and MIL-101(Cr). HIAM-410 and the aforementioned three compounds were treated with boiling water for 1 week and their crystallinity and porosity were evaluated afterwards. It was observed that the PXRD patterns of HIAM-410, UiO-66, and MIL-101(Cr) after boiling water treatments matched well with those of their pristine samples, indicating the full preservation of their structural integrity during the process (Figure 3b and Figure S8). Importantly, no notable loss of porosity was observed for the three compounds after the treatments, as suggested by N_2 adsorption results (Figure 3a and Figure S9). In contrast, the crystallinity and porosity of UiO-67 were totally lost after the boiling water treatments, suggesting that its structure is less stable compared to the other three materials. The pH values of the water solutions before and after the treatments were subsequently measured for HIAM-410, UiO-66, and MIL-101(Cr) to detect possible degradation of the crystal structure and release of carboxylate linkers. The results indicated the pH values of the water solutions after treatments with HIAM-410, UiO-66, and MIL-101(Cr) were 5.60, 4.45, and 3.85, respectively, slightly lower than that of the original water (pH 6.5), indicating the high hydrothermal stability of the adsorbents.

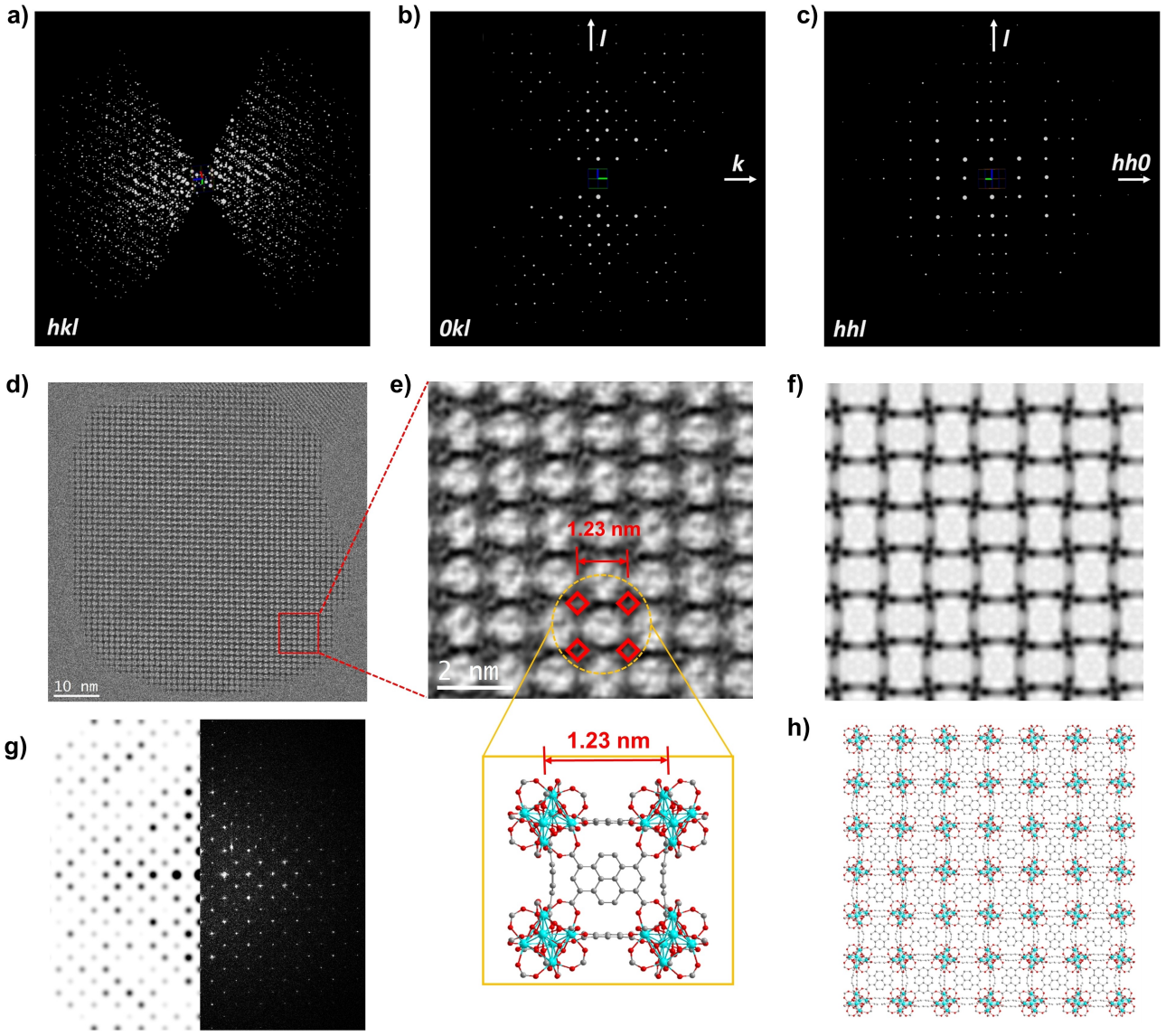

Figure 2. 3D reciprocal lattice of HIAM-410 and its low-dose HRTEM imaging. a) Reconstructed 3D reciprocal lattice of HIAM-410 from the cRED data. b) and c) Two-dimensional slices *0kl* and *hhl* extracted from the reconstructed reciprocal lattice. The reflection conditions deduced from the 3D reciprocal lattice and the 2D slices of *0kl* and *hhl* are *hkl*: $h+k+l=2n$; *0kl*: $k+l=2n$; *hhl*: $l=2n$; *00l*: $l=2n$. The possible space groups are *I*23, $I2_13$, *Im*-3, *I*432, *I*-43*m*, and *Im*-3*m*. d) HRTEM image of HIAM-410, acquired along the $<001>$ zone axis. e) Contrast transfer function (CTF)-corrected image of the marked area in (d). f) Simulated projected potential map along the $<001>$ direction of HIAM-410VF with a point spread function width of 2 Å. g) Left: simulated electron diffraction (ED) pattern along $\langle 001 \rangle$ direction, Right: Fourier transform image of (d). h) View of crystal structure of HIAM-410VF along the *a*-axis.

A rough estimation (using UiO-66 as an example) suggested that the linker leaching percentage is less than 1% after boiling water treatments.

The highly robust HIAM-410 was evaluated for the adsorption and separation of hexane isomers with different degrees of branching, including linear n-hexane (nHEX), monobranched 3-methylpentane (3MP), and dibranched 2,2-dimethylbutane (22DMB). At 30 °C and a relative pressure of $P/P_0=0.5$, HIAM-410 can take up all three adsorbates with adsorption capacities of 121, 111, and 103 mg/g for nHEX, 3MP, and 22DMB, respectively. In addition, none of the three isomers exhibit notable diffusional restrictions (Figure 4c). This seems contradictory to the pore dimensions of HIAM-410 which has a pore aperture of ≈4 Å from the crystal structure, and ab initio calculations indicated that HIAM-410VF, without linker vacancies, would not accommodate any of the hexane isomers (kinetic diameter: nHEX: 4.3 Å, 3MP: 5.5 Å, 22DMB: 6.2 Å) as a result of the high energy barrier to pass through the narrow window. It should be noted that the calculation was performed on a perfect 4,12-connected structure without defect sites. However, the adsorption results were not surprising considering the high degree of defects in the crystal structure, which notably enlarged the effective pore dimensions of the material. The effective pore aperture could be as large as 8 Å at the linker vacancy site. Adsorption isotherms of nHEX, 3MP, and

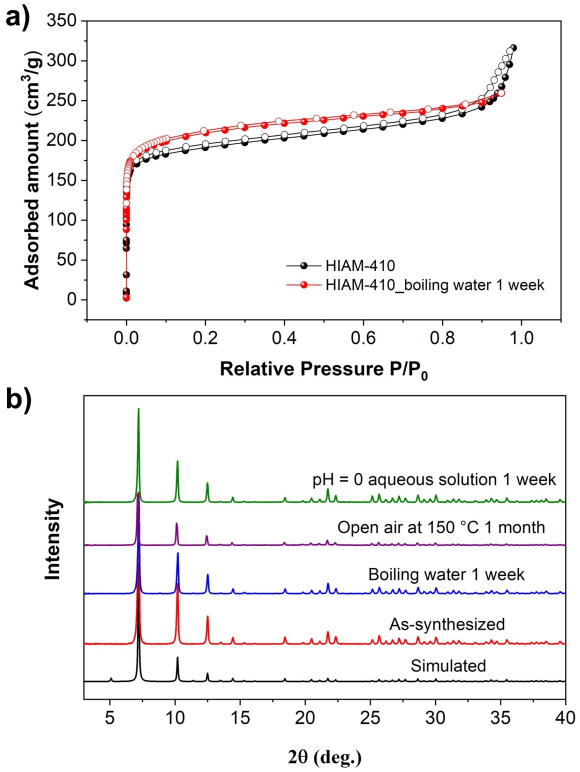

Figure 3. Porosity and stability of HIAM-410. a) N_2 adsorption-desorption isotherm at 77 K by pristine HIAM-410 (black) and HIAM-410 after boiling water treatment for 1 week (red). b) PXRD patterns of HIAM-410 under various treatments comparing with the simulated one.

22DMB by HIAM-410 were collected at 30, 90, and 150 °C (Figure S10–S12). While all three isomers can diffuse freely into the structure of HIAM-410, they display different adsorption capacities and affinity, both with a sequence of nHEX > 3MP > 22DMB. At 30 °C, the adsorption capacities for nHEX, 3MP, and 22DMB are 129, 107, and 89 mg g^{-1} at 20 kPa, and the values at 150 °C are 84, 82, and 62 mg g^{-1}, respectively. The calculated isosteric heats of adsorption (Q_{st}) demonstrated that the initial values for nHEX, 3MP, and 22DMB are 90.1, 55.3, and 27.9 kJ mol^{-1} at low loading, in accordance with that of the adsorption capacities (Figure S17). Multicomponent column breakthrough measurements were performed to evaluate the separation capability of HIAM-410, with a feed of equimolar ternary mixture of nHEX, 3MP, and 22DMB. At 30 °C, the compound is capable of discriminating the three isomers, with the breakthrough time of 178, 234, and 312 min g^{-1} for 22DMB, 3MP, and nHEX, respectively (Figure 4e). This is consistent with the sequence of adsorption capacities and adsorption affinity, which leads to a thermodynamically controlled separation. The selectivity (ratio of breakthrough time) of 3MP/22DMB is 1.31, comparable to that of other MOFs showing thermodynamic separation of the isomers such as $Fe_2(BDP)_3$ (≈1.1) and Zr-abtc (≈1.3).[33,35] However, when the temperature increased to industrially more relevant temperature (150 °C), HIAM-410 can barely separate the isomers of different branching. 22DMB eluted out first followed by the co-breakthrough of nHEX and 3MP (Figure S18). These results demonstrate that HIAM-410 is capable of discriminating hexane isomers as a result of their different adsorption affinity, but with relatively low selectivity and separation efficiency.

The relatively poor separation capability of HIAM-410 should be attributed to its high rate of linker vacancies, leading to the notably enlarged effective pore dimension that allows for the free passage of all the aforementioned hexane isomers. Thus the separation relied merely on the tiny difference in adsorption affinity between different adsorbates. This prompted us to explore the possibility of improving the separation ability of the material by engineering its linker vacancies through the post-synthetic linker insertion. Pore engineering of MOFs by the linker installation has been well-documented for ordered "pockets" and dicarboxylates. For example, Zhou et al. demonstrated linear dicarboxylate linkers with different functional groups can be sequentially installed at the linker vacancy sites of the **bcu**-type Zr-Me_2-BPDC built on 8-connected Zr_6 node. However, linker insertion at randomly distributed defect sites with tetracarboxylates has not been well explored. Post-synthetic insertion of ptc^{4-} in HIAM-410 was carried out through further solvothermal reaction of as-synthesized HIAM-410 and excess H_4ptc at 100 °C. The obtained crystalline product was washed thoroughly with DMF and methanol to remove residual organic linkers, and is denoted as HIAM-410LI (HIAM-410 with ligand insertion). PXRD analysis revealed the pattern of HIAM-410LI remained essentially the same as that of the pristine compound, indicating the overall structure was fully preserved (Figure 4a). The comparison of TGA curves of HIAM-410 and HIAM-410LI suggested that the latter has a smaller initial weight loss associated with free solvents and a higher weight percent of organic linkers (Figure S5). These results implied that the linker vacancies may be, at least partially, restored through the post-synthetic process. To quantitatively assess the linker vacancies in HIAM-410LI, its crystal structure was re-evaluated through Rietveld refinement against PXRD data. Indeed, the overall connectivity and atomic coordination of HIAM-410LI remained intact compared to that of HIAM-410, however, we did observe an increase of linker occupancy from 81.5 % to 88.0 %. This suggests that the linker vacancies were partially restored by the post-synthetic linker installation, and the defect rate decreased from 18.5 % to 12 %. The results were further supported by elemental analysis where an increase of C (%) and a decrease of O (%) were observed upon linker insertion (Supporting Information Table S4), in consistent with the X-ray diffraction data as well as the experimental adsorption results which will be presented later on. N_2 adsorption at 77 K by HIAM-410LI displayed a decrease in adsorption capacity (Figure 4b), resulting in a BET surface area of 616 m^2 g^{-1}, slightly lower than that of HIAM-410 (823 m^2 g^{-1}). This is reasonable considering the increased occupancy of the organic linker.

We speculated the successful linker installation may lead to the contraction of the accessible pore aperture of the structure, which prompted us to evaluate the separation

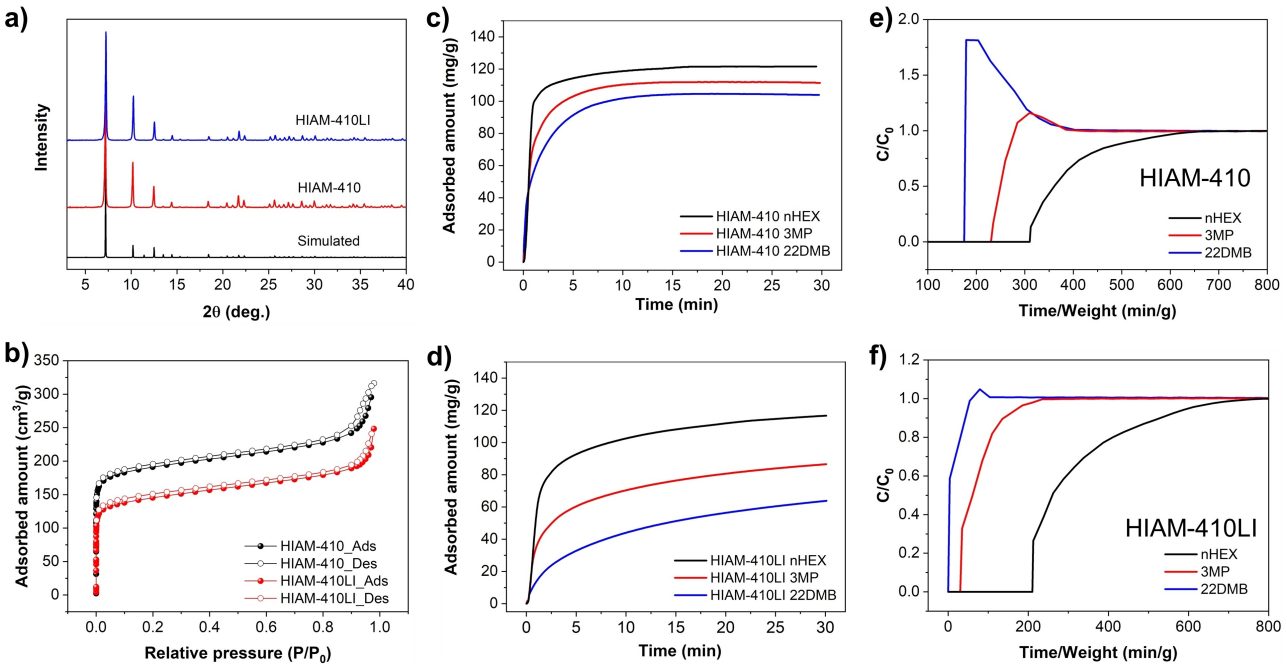

Figure 4. Hexane isomers separation. a) Comparison of the PXRD patterns of HIAM-410, HIAM-410LI and the simulated pattern of HIAM-410VF. b) N_2 adsorption-desorption isotherms at 77 K by HIAM-410 (black) and HIAM-410LI (red). c) Adsorption of nHEX, 3MP, and 22DMB at 30 °C and 50 torr by HIAM-410. d) Adsorption of nHEX, 3MP, and 22DMB at 30 °C and 50 torr by HIAM-410LI. e) Column breakthrough curve for an equimolar ternary mixture of nHEX, 3MP, and 22DMB at 30 °C by HIAM-410. f) Column breakthrough curve for an equimolar ternary mixture of nHEX, 3MP, and 22DMB at 30 °C by HIAM-410LI.

capability of HIAM-410LI. Adsorption of nHEX, 3MP, and 22DMB by HIAM-410LI at 30 °C revealed that the adsorption rates were notably lower than that for HIAM-410 (Figure 4d). In particular, 3MP and 22DMB displayed evident diffusion restrictions. The adsorption rates of nHEX, 3MP, and 22DMB are 123.1, 74.6, and 17.9 $mg\,g^{-1}\,min^{-1/2}$, respectively (Figure S13). Adsorption isotherms of the three isomers by HIAM-410LI were measured at 30, 90, and 150 °C, with sufficient equilibrium time (Figure S14–S16). In general, the adsorption capacities of HIAM-410LI for all adsorbates are lower than those of HIAM-410. This is reasonable considering its decreased porosity upon linker insertion. In addition, the adsorption amounts in HIAM-410LI follow the sequence of nHEX > 3MP > 22DMB, similar to that observed for HIAM-410. The heats of adsorption for nHEX, 3MP, and 22DMB are 100.5, 64.4, and 41.3 $kJ\,mol^{-1}$, respectively at low loading (Figure S17). The notable differences in adsorption kinetics as well as adsorption affinity implied HIAM-410LI may be capable of efficient separation of hexane isomers. This was further validated by column breakthrough measurements with a feed of equimolar nHEX, 3MP, and 22DMB. The breakthrough curves at 30 °C demonstrated that 22DMB eluted out from the column at the very beginning of the measurement, suggesting its full exclusion by the adsorbent under dynamic multicomponent adsorption conditions (Figure 4f). This was followed by the breakthrough of 3MP and nHEX which occurred at the 34th and 212th $min\,g^{-1}$, respectively. The results suggest that, upon linker vacancy engineering, HIAM-410LI is able to fully separate linear/monobranched and dibranched hexane isomers. More importantly, further breakthrough test at 150 °C revealed the separation capability of HIAM-410LI was fully retained, showing efficient splitting of hexane isomers as a function of branching (Figure S19). This is a significant enhancement as full separation of monobranched and dibranched alkane isomers by porous solids through size-exclusion is crucial in the industry, but has rarely been reported.[36,37] In particular, previous studies for full splitting of monobranched and dibranched alkane isomers were mostly evaluated at ambient temperature, while in this work we demonstrated the capability of HIAM-410LI for the separation at industrially more relevant temperature.[36–39] We believe the excellent separation capability of HIAM-410LI should be attributed to a synergistic effect of thermodynamically and kinetically controlled mechanisms. However, the distinct adsorption kinetics of the isomers resulted from linker insertion may be the main reason.

Conclusion

Efficient separation of alkane isomers remains a challenge in petrochemical industry. The discrimination of physically and chemically similar alkane molecules requires precise engineering of the pore structure and chemistry of the adsorbents to achieve optimal separation efficiency. In this regard, MOFs are particularly promising as their rich chemistry, diverse structure, and highly tunable pore dimensions allow fine tailoring of their structural details and

optimization of the separation capability. The MOF structure we reported in this work, HIAM-410 built on 12-connected Zr_6 nodes and a 4-connected tetracarboxylate linker, possesses a **ftw** network. The compound demonstrates exceptional thermal and water stability which is comparable to that of the prototype MOFs including MIL-101(Cr) and UiO-66. Interestingly, the pristine HIAM-410 possesses nearly 18.5 % of linker vacancy sites that could be partially restored via post-synthetic linker insertion forming HIAM-410LI, which demonstrates notably improved separation capability for hexane isomers. Upon the linker installation, HIAM-410LI can completely separate monobranched and dibranched hexane isomers, as demonstrated by the multicomponent column breakthrough measurements at 30 and 150 °C. Our study serves as a good example illustrating the great promise of MOFs for challenging separation processes, where pore structures could be finely engineered to achieve optimal separation efficiency.

Acknowledgements

We thank the financial support from the Shenzhen Science and Technology Program (No. RCYX20200714114539243, KCXFZ20211020163818026).

Conflict of Interest

The authors declare no conflict of interest.

Data Availability Statement

The data that support the findings of this study are available in the Supporting Information of this article.

Keywords: Adsorption · Alkane Isomers · Metal-Organic Frameworks · Separation

[1] Y. Wu, B. M. Weckhuysen, *Angew. Chem. Int. Ed.* **2021**, *60*, 18930–18949.
[2] D. Peralta, G. Chaplais, A. Simon-Masseron, K. Barthelet, G. D. Pirngruber, *Ind. Eng. Chem. Res.* **2012**, *51*, 4692–4702.
[3] A. Molaei Dehkordi, M. Khademi, *Microporous Mesoporous Mater.* **2013**, *172*, 136–140.
[4] D. S. Sholl, R. P. Lively, *Nature* **2016**, *532*, 435–437.
[5] H. Furukawa, K. E. Cordova, M. O'Keeffe, O. M. Yaghi, *Science* **2013**, *341*, 1230444.
[6] L. Yang, S. Qian, X. Wang, X. Cui, B. Chen, H. Xing, *Chem. Soc. Rev.* **2020**, *49*, 5359–5406.
[7] C. Jansen, N. Assahub, A. Spieß, J. Liang, A. Schmitz, S. Xing, S. Gökpinar, C. Janiak, *Nanomaterials* **2022**, *12*, 3614.
[8] A. Cadiau, K. Adil, P. M. Bhatt, Y. Belmabkhout, M. Eddaoudi, *Science* **2016**, *353*, 137–140.
[9] H. Zeng, M. Xie, T. Wang, R.-J. Wei, X.-J. Xie, Y. Zhao, W. Lu, D. Li, *Nature* **2021**, *595*, 542–548.
[10] B. Liang, X. Zhang, Y. Xie, R.-B. Lin, R. Krishna, H. Cui, Z. Li, Y. Shi, H. Wu, W. Zhou, B. Chen, *J. Am. Chem. Soc.* **2020**, *142*, 17795–17801.
[11] L. Yu, X. Han, H. Wang, S. Ullah, Q. Xia, W. Li, J. Li, I. da Silva, P. Manuel, S. Rudić, Y. Cheng, S. Yang, T. Thonhauser, J. Li, *J. Am. Chem. Soc.* **2021**, *143*, 19300–19305.
[12] R.-B. Lin, L. Li, H.-L. Zhou, H. Wu, C. He, S. Li, R. Krishna, J. Li, W. Zhou, B. Chen, *Nat. Mater.* **2018**, *17*, 1128–1133.
[13] Z. Bao, J. Wang, Z. Zhang, H. Xing, Q. Yang, Y. Yang, H. Wu, R. Krishna, W. Zhou, B. Chen, Q. Ren, *Angew. Chem. Int. Ed.* **2018**, *57*, 16020–16025.
[14] L. Li, L. Guo, D. H. Olson, S. Xian, Z. Zhang, Q. Yang, K. Wu, Y. Yang, Z. Bao, Q. Ren, J. Li, *Science* **2022**, *377*, 335–339.
[15] H.-L. Xia, K. Zhou, L. Yu, H. Wang, X.-Y. Liu, D. M. Proserpio, J. Li, *Inorg. Chem.* **2022**, *61*, 7980–7988.
[16] M. Eddaoudi, J. Kim, N. Rosi, D. Vodak, J. Wachter, M. Keeffe, O. M. Yaghi, *Science* **2002**, *295*, 469.
[17] H. Deng, S. Grunder, K. E. Cordova, C. Valente, H. Furukawa, M. Hmadeh, F. Gándara, A. C. Whalley, Z. Liu, S. Asahina, H. Kazumori, M. O'Keeffe, O. Terasaki, J. F. Stoddart, O. M. Yaghi, *Science* **2012**, *336*, 1018–1023.
[18] J. H. Cavka, S. Jakobsen, U. Olsbye, N. Guillou, C. Lamberti, S. Bordiga, K. P. Lillerud, *J. Am. Chem. Soc.* **2008**, *130*, 13850–13851.
[19] S. J. Geier, J. A. Mason, E. D. Bloch, W. L. Queen, M. R. Hudson, C. M. Brown, J. R. Long, *Chem. Sci.* **2013**, *4*, 2054–2061.
[20] H. Wang, X. Dong, V. Colombo, Q. Wang, Y. Liu, W. Liu, X.-L. Wang, X.-Y. Huang, D. M. Proserpio, A. Sironi, Y. Han, J. Li, *Adv. Mater.* **2018**, *30*, 1805088.
[21] X. Li, J. Liu, K. Zhou, S. Ullah, H. Wang, J. Zou, T. Thonhauser, J. Li, *J. Am. Chem. Soc.* **2022**, *144*, 21702–21709.
[22] Y. Chen, X. Zhang, M. R. Mian, F. A. Son, K. Zhang, R. Cao, Z. Chen, S.-J. Lee, K. B. Idrees, T. A. Goetjen, J. Lyu, P. Li, Q. Xia, Z. Li, J. T. Hupp, T. Islamoglu, A. Napolitano, G. W. Peterson, O. K. Farha, *J. Am. Chem. Soc.* **2020**, *142*, 21428–21438.
[23] J. Pang, S. Yuan, J. Qin, C. Liu, C. Lollar, M. Wu, D. Yuan, H.-C. Zhou, M. Hong, *J. Am. Chem. Soc.* **2017**, *139*, 16939–16945.
[24] Q.-G. Zhai, X. Bu, X. Zhao, D.-S. Li, P. Feng, *Acc. Chem. Res.* **2017**, *50*, 407–417.
[25] Y. Wang, X. Jia, H. Yang, Y. Wang, X. Chen, A. N. Hong, J. Li, X. Bu, P. Feng, *Angew. Chem. Int. Ed.* **2020**, *59*, 19027–19030.
[26] S. Yuan, W. Lu, Y.-P. Chen, Q. Zhang, T.-F. Liu, D. Feng, X. Wang, J. Qin, H.-C. Zhou, *J. Am. Chem. Soc.* **2015**, *137*, 3177–3180.
[27] S. Yuan, Y.-P. Chen, J.-S. Qin, W. Lu, L. Zou, Q. Zhang, X. Wang, X. Sun, H.-C. Zhou, *J. Am. Chem. Soc.* **2016**, *138*, 8912–8919.
[28] M. J. Katz, Z. J. Brown, Y. J. Colon, P. W. Siu, K. A. Scheidt, R. Q. Snurr, J. T. Hupp, O. K. Farha, *Chem. Commun.* **2013**, *49*, 9449–9451.
[29] O. V. Gutov, M. G. Hevia, E. C. Escudero-Adán, A. Shafir, *Inorg. Chem.* **2015**, *54*, 8396–8400.
[30] X. Wang, L. Zhai, Y. Wang, R. Li, X. Gu, Y. D. Yuan, Y. Qian, Z. Hu, D. Zhao, *ACS Appl. Mater. Interfaces* **2017**, *9*, 37848–37855.
[31] K. B. Idrees, Z. Chen, X. Zhang, M. R. Mian, R. J. Drout, T. Islamoglu, O. K. Farha, *Chem. Mater.* **2020**, *32*, 3776–3782.
[32] Y. Bai, Y. Dou, L.-H. Xie, W. Rutledge, J.-R. Li, H.-C. Zhou, *Chem. Soc. Rev.* **2016**, *45*, 2327–2367.
[33] H. Wang, X. Dong, J. Lin, S. J. Teat, S. Jensen, J. Cure, E. V. Alexandrov, Q. Xia, K. Tan, Q. Wang, D. H. Olson, D. M. Proserpio, Y. J. Chabal, T. Thonhauser, J. Sun, Y. Han, J. Li, *Nat. Commun.* **2018**, *9*, 1745.
[34] Y. Wang, S. Takki, O. Cheung, H. Xu, W. Wan, L. Öhrström, A. K. Inge, *Chem. Commun.* **2017**, *53*, 7018–7021.

[35] Z. R. Herm, B. M. Wiers, J. A. Mason, J. M. van Baten, M. R. Hudson, P. Zajdel, C. M. Brown, N. Masciocchi, R. Krishna, J. R. Long, *Science* **2013**, *340*, 960–964.
[36] L. Yu, X. Dong, Q. Gong, S. R. Acharya, Y. Lin, H. Wang, Y. Han, T. Thonhauser, J. Li, *J. Am. Chem. Soc.* **2020**, *142*, 6925–6929.
[37] L. Yu, S. Ullah, H. Wang, Q. Xia, T. Thonhauser, J. Li, *Angew. Chem. Int. Ed.* **2022**, *61*, e202211359.
[38] L. Yu, S. Ullah, K. Zhou, Q. Xia, H. Wang, S. Tu, J. Huang, H.-L. Xia, X.-Y. Liu, T. Thonhauser, J. Li, *J. Am. Chem. Soc.* **2022**, *144*, 3766–3770.
[39] Z. Zhang, S. B. Peh, C. Kang, K. Yu, D. Zhao, *Angew. Chem. Int. Ed.* **2022**, *61*, e202211808.

Manuscript received: March 9, 2023
Accepted manuscript online: April 22, 2023
Version of record online: ■■, ■■

Research Articles

Gas Separation

F.-A. Guo, J. Wang, C. Chen, X. Dong, X. Li, H. Wang,* P. Guo,* Y. Han, J. Li* e202303527

Linker Vacancy Engineering of a Robust ftw-type Zr-MOF for Hexane Isomers Separation

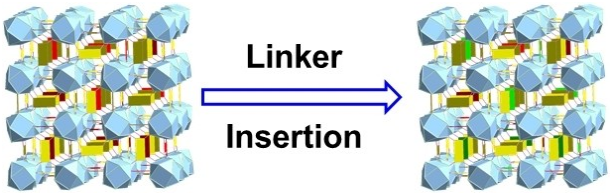

A highly robust **ftw**-type zirconium-based metal–organic framework has been constructed. Its linker vacancy sites are restored by post-synthetic linker insertion, which notably enhances its separation performance toward alkane isomers.